Isolated Diatomic Ni-Fe Metal-Nitrogen Sites for Synergistic Electroreduction of CO_2

*Wenhao Ren,† Xin Tan,† Wanfeng Yang, Chen Jia, Sean C. Smith and Chuan Zhao**

Abstract: Polynary single-atom structures can integrate the advantage of homogeneous and heterogeneous catalysts while providing synergistic functions based on different molecules and their interfaces. However, the fabrication and identification of such active site prototype remain elusive. Here we report isolated diatomic Ni-Fe sites anchored on nitrogenated carbon as an efficient electrocatalyst for CO_2 reduction. The catalyst exhibits high selectivity with CO Faradaic efficiency above 90% over a wide potential range from -0.5 to -0.9 V (98% at -0.7 V), and robust durability with 99% of its initial selectivity after 30 hours of electrolysis. Density functional theory studies reveal that the neighbouring Ni-Fe centers not only function in synergy to decrease the reaction barrier for the formation of COOH* and desorption of CO, but also undergo distinct structural evolution into a CO-adsorbed moiety upon CO_2 uptake.

Electrochemical reduction of CO_2 into value-added products provides a promising strategy to realize a carbon-neutral energy circulation.[1] However, the stable C=O bond (806 kJ mol^{-1}) in CO_2 and the competing hydrogen evolution reaction (HER) render that a single catalytic system must optimize the interplay among selectivity, activity and stability.[2] Single-atom catalysts (SACs) with fully exposed, high selectivity and well-defined active sites have manifested great potential to tackle these challenges in CO_2 reduction reaction (CO_2RR).[3]

A good example is the atomically dispersed transition metals (e.g. Ni, Fe, Co) anchored on nitrogenated carbon, which has demonstrated impressive activity for CO_2RR to CO.[4] The overall conversion process is proposed to occur in three steps: (*i*) $CO_2 + H^+ + e^- \rightarrow COOH^*$; (*ii*) $COOH^* + H^+ + e^- \rightarrow CO^* + H_2O$; (*iii*) $CO^* \rightarrow CO + *$.[5] It is revealed that the Ni-N sites exhibit high current density for CO production, but suffer from sluggish kinetics of the first proton-coupled electron transfer (Step *i*).[6] The Fe-N and Co-N show low onset potential for CO_2RR, whereas the desorption of *CO into the gas phase lowers their reactivity due to the strong binding of CO to the single Fe or Co atom site (Step *iii*).[7] These limitations generally arise from the simplicity of the single-atom center which is only capable of catalyzing single-molecule elementary reactions.[8] This presents significant challenges to electrocatalytic CO_2RR that involves multiple intermediates and products. To address these issues, one strategy is to build polynary single-atom structures (e.g. between two or more atoms with different chemical identities) with exposed atomic interfaces, synergistic interactions and more sophisticated functionalities. Such design can maximize the potentials of SACs for multistep catalytic reactions that require the presence of active sites with different functionalities simultaneously.

Herein, we report a diatomic metal-nitrogen site (Ni/Fe-N-C), through an ionic exchange strategy based on the pyrolysis of Zn/Ni/Fe zeolitic imidazolate framework for efficient CO_2RR. The diatomic configuration and coordination path of catalyst are uncovered by aberration-corrected scanning transmission electron microscopy (STEM) and X-ray absorption spectroscopy (XAS). Experimental results and density functional theory (DFT) calculations reveal that the reaction barrier decreases significantly in Ni-Fe dual center in comparison to simplex Ni or Fe center. Consequently, the Ni/Fe-N-C facilitates electrocatalytic CO_2RR by showing an ultrahigh Faradaic efficiency of 98% at -0.7 V, outstanding turnover frequency, as well as robust electrode durability.

Isolated diatomic metal-nitrogen catalyst was synthesized by a metal-organic framework (MOF) assisted method (Figure S1). The Fe doped zeolitic imidazolate frameworks-8 (ZIF-8) was first fabricated by mixing zinc nitrate, iron nitrate, and 2-methylimidazole based on an established approach.[9] Instead of physically absorbed in the cavities of ZIF-8, Fe-ions are chemically bonded with the organic ligand as nodes, hence ensuring atomic dispersion of Fe in precursor. Afterward, the Fe doped ZIF-8 was dispersed in n-hexane homogeneously, followed by the dropwise injection of nickel nitrate methanol solution. By virtue of this dual-solvent route, the nickel nitrate could be encapsulated within the small ZIF-8 cavities ($<$ 5 Å, Figure S2).[10] X-ray diffraction (XRD) analysis indicates that the Fe and Ni co-doped precursors possess similar crystal pattern to ZIF-8 (Figure S3). Finally, the volatilization of low boiling point Zn nodes (907 °C) took place during the thermal treatment at 1000 °C, and nitrogen coordinated Ni and Fe diatomic catalyst (Ni/Fe-N-C) was obtained. For comparison, pure Ni-N-C and Fe-N-C were also synthesized through the similar method (Figure S4 and Figure S5).

As revealed by scanning electron microscopy (SEM, Figure 1a), the as-prepared Ni/Fe-N-C is uniform in size (50-100 nm), maintaining the initial rhombic dodecahedron shapes with distinct edges after thermal treatment. Closer observations in high-angle annular dark-field scanning transmission electron microscopy (HAADF-STEM) image indicate that there is no metal nanoparticle formed (Figure 1b). Figure 1c shows the selected area electron diffraction (SAED) of Ni/Fe-N-C with the annular patterns, corresponding merely to the characteristic of amorphous carbon. From the aberration-corrected high-resolution HAADF-STEM image (Figure 1d), the existence of Ni and Fe single-atoms is observed in form of homogeneously distributed bright spots. Besides, many neighbouring dual-dots

Dr. Wenhao Ren, Wanfeng Yang, Chen Jia, Prof. Chuan Zhao
School of Chemistry, University of New South Wales, Sydney, New South Wales 2052, Australia
E-mail: chuan.zhao@unsw.edu.au
Dr. Xin Tan, Prof. Sean C. Smith State Department of Applied Mathematics, Research School of Physics and Engineering, The Australian National University, Canberra, ACT 2601, Australia

Supporting information for this article is given via a link at the end of the document.

are uncovered in Figure 1e, which suggests the formation of diatomic atom sites. The elemental distribution was elucidated by energy-dispersive X-ray spectroscopy (EDS) analysis, where Ni, Fe, and N were evenly dispersed on the carbon matrix (Figure 1f).

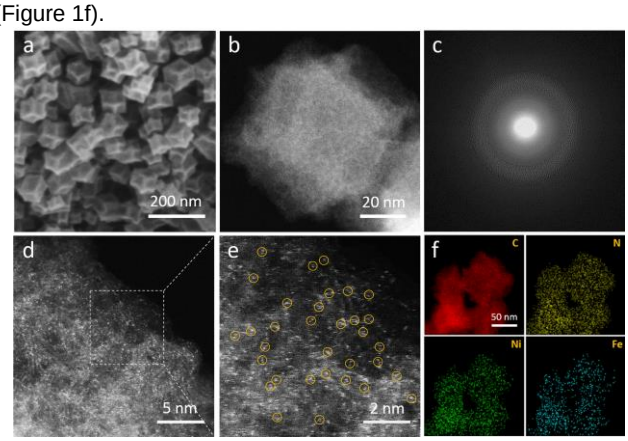

Figure 1. a) SEM image, b) HAADF-STEM image, c) SAED patterns of Ni/Fe-N-C. d,e) Zoom-in HAADF-STEM images of Ni/Fe-N-C. f) Elemental mapping of Ni/Fe-N-C.

X-ray photoelectron spectroscopy (XPS) was then used to characterize the catalyst surface and composition. The high-resolution N 1s spectra of all the samples evidenced the presence of pyridinic (398.6 eV), pyrrolic (401.1 eV), graphitic (402.2 eV), and N-O_x (403.5 eV) species (Figure 2a).[11] Notably, other than the bare N-C sample, Ni/Fe-N-C, Ni-N-C, and Fe-N-C all show the metal-coordinated (M-N) porphyrin-like moieties (399.6 eV). The peak area of Ni/Fe-N is significantly larger than Ni-N and Fe-N, indicating the formation of bimetal-nitrogen sites. Figure 2b shows the XRD analysis of the samples, from which the Ni/Fe-N-C, Ni-N-C, and Fe-N-C show similar diffraction patterns with broad graphite peaks, implying the absence of Ni and Fe nanoparticles (NPs), consistent with the SEM and HAADF-STEM results. Further increasing the content of adsorbed nickel nitrate, two well-defined Ni peaks emerged at 44.1° and 51.6° after calcination, indicating the agglomeration of Ni clusters into nanoparticles (Figure S6).

The Ni K edge X-ray absorption near-edge structure (XANES) of Ni/Fe-N-C and Ni-N-C compared with standard Ni-Pc and Ni-foil are shown in Figure 2c. The near-edge of Ni/Fe-N-C and Ni-N-C sites between those of Ni-foil and Ni-Pc, suggesting that the average valence state of Ni is in intermediate Ni(0) and Ni(II).[10a] The inset of Figure 2c highlights the pre-edge features at approximately 8,334 eV, which signals 3d and 4p orbital hybridization of the Ni central atoms. The increased peak intensity in Ni/Fe-N-C, compared with Ni-N-C and Ni-Pc, is ascribed to the distorted D_{4h} symmetry.[6,12] This result certifies that Ni species in Ni/Fe-N-C exhibit a similar coordination path between metal centers and pyridinic/pyrrolic N, but the D_{4h} symmetry was distorted by another coordination path such as metal-metal. Figure 2d displays the Fourier transform (FT) k^2-weighted $\chi(k)$ function of the extended X-ray absorption fine structure (EXAFS) spectra. The peaks at 1.30 Å and 2.06 Å can be assigned to the metal-nitrogen and metal-metal path, respectively.[13] The major peak for Ni/Fe-N-C and Ni-N-C at 1.30 Å verifies the dominant Ni-N coordination. Note that there is an obvious metal-metal path for Ni/Fe-N-C at 2.06 Å, which cannot be found in pure Ni-N-C and Fe-N-C, corroborating the formation of Ni-Fe coordination. To further identify the Ni-Fe

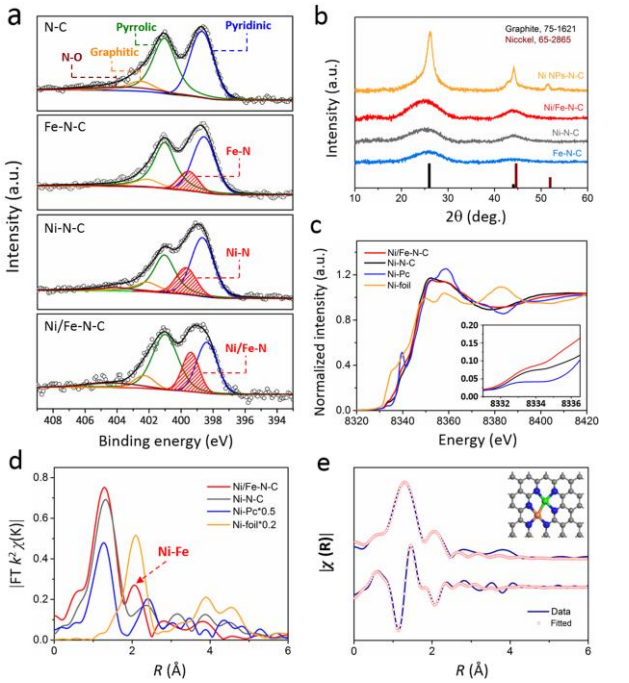

Figure 2. a) High-resolution XPS N 1s spectrum of samples. b) XRD patterns. c) Ni K-edge XANES spectra of Ni/Fe-N-C, Ni-N-C, Fe-N-C, and Ni-foil. d) Fourier transformation of the EXAFS spectra at R space. e) The first two shell (Ni-N, Ni-Fe) fitting of Fourier transformations of EXAFS spectra for Ni/Fe-N-C.

path, density functional theory (DFT) was used to deduce the possible bimetal-nitrogen models based on the EXAFS experimental spectra and fitted FT curves (Table S2). The calculated Ni-Fe path in Figure 2e fits well with the experimental spectra at 2.06 Å. Besides, the Fe K edge XANES also shows the metal-metal path, and the fitting results were in good agreement with the same model (Figure S8). Other coordination structures can be excluded by comparing the fitting results to K-edge EXAFS spectra (Figure S9). By contrast, dispersion of Fe-N_4 and Ni-N_4 was prevailing due to the deficiency of a metal-metal path (Figure S10).

Electrochemical reduction of CO_2 was first conducted by linear sweep voltammetry (LSV) in a H-cell. As shown in Figure 3a, Ni/Fe-N-C exhibits superior activity in CO_2-saturated 0.5 M $KHCO_3$ electrolyte, giving a current density of 31.6 mA cm^{-2} at -1.1 V (vs. RHE), significantly exceeding that of the Fe-N-C and Ni-N-C, respectively, suggesting a strong synergistic effect between Ni and Fe in bimetal sites. A much smaller current density and higher onset potential were observed when tested in Ar-saturated $KHCO_3$ electrolyte, indicating the excellent activity of Ni/Fe-N-C stemmed from CO_2 reduction. The liquid and gas products were analyzed by off-line nuclear magnetic resonance spectroscopy and on-line gas chromatography, which indicate

H_2 and CO are the only two products of the reaction (Figure S12). Figure 3b presents the FE of CO generation from three catalysts. Among them, Fe-N-C and Ni-N-C reach their maximum FE at different potentials of -0.5 V and -0.8 V, respectively, which is attributed to the different reaction kinetics (will be elaborated later). Note that the FE of Ni/Fe-N-C outperforms Fe-N-C and Ni-N-C across the entire potential

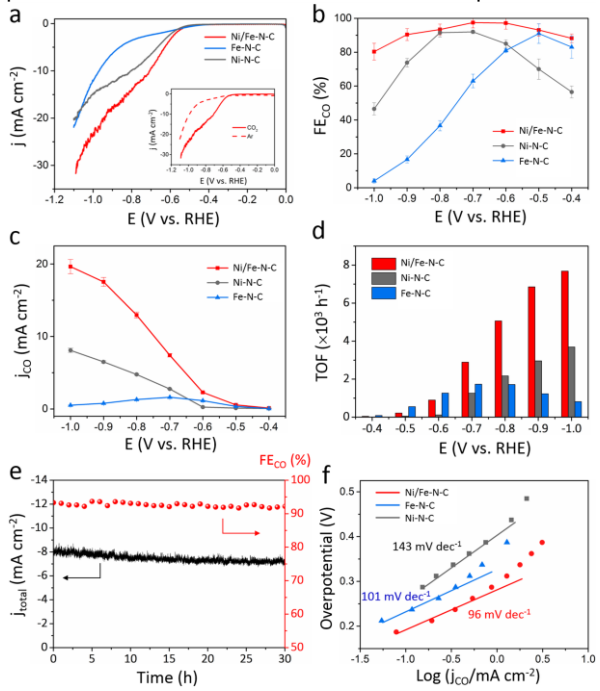

Figure 3. a) LSV curves obtained in CO_2-saturated 0.5 M $KHCO_3$ solution. Inset is the LSV comparison for Ni/Fe-N-C in Ar- and CO_2-saturated 0.5 M $KHCO_3$ solution. b) FE_{CO}, c) j_{CO}, and d) TOF of Ni/Fe-N-C, Ni-N-C, Fe-N-C at various applied potentials. e) Stability test for Ni/Fe-N-C at -0.7 V. f) Tafel plots of the samples.

window from -0.4 to -1.0 V, reaching a maximum FE of 98% at -0.7 V. Figure 3c shows the dependence of the CO current density on applied potential. The current density of Ni/Fe-N-C increases acutely with increased applied potential and reaches up to 19.7 mA cm^{-2} at -1.0 V, two times higher than Ni-N-C at the same potential. Meanwhile, the small CO current density of Fe-N-C is due to its low FE at high overpotential. The intrinsic activity of catalyst is further disclosed by the calculation of TOF based on the number of metal involved in the reaction (Figure 3d). The calculated TOFs at a potential of -1.0 V for Ni/Fe-N-C, Ni-N-C, and Fe-N-C are 7682, 3690 and 813 h^{-1}, respectively, indicating the highly enhanced activity of bimetal-nitrogen sites.Moreover, Ni/Fe-N-C also exhibits outstanding durability for CO_2RR, maintaining 99% of the initial FE for CO production (~ 8 mA cm^{-2}) after 30 hours of continuous electrolysis (Figure 3e).

To understand the origin of high catalytic activity of Ni/Fe-N-C catalyst, the electrochemical active surface area (ECSA) estimated from the double-layer capacitance (C_{dl}) and Nyquist plots were then investigated for Ni/Fe-N-C, Ni-N-C, and Fe-N-C (Figure S14). All the samples exhibit similar C_{dl} (15.1 ~ 18.7 mF cm^{-2}) and charge transfer resistance (4 ~ 6 Ω), which suggests that rather than the surface area (number of active sites) or electrical conductivity, the activity of each site in the catalyst dominates the CO_2RR process. To uncover the reaction kinetics of different sites, Tafel plots were further carried out and analyzed. Tafel slopes of 96, 101, and 143 mV $decade^{-1}$ were fitted for Ni/Fe-N-C, Fe-N-C, and Ni-N-C, respectively (Figure 3f). This reveals that the first electron transfer, which generates surface adsorbed *COOH intermediate, is the rate-determining

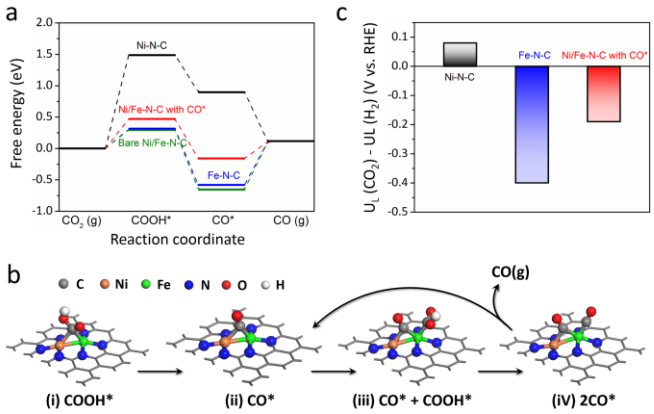

Figure 4. a) The calculated free energy diagrams for CO_2RR to CO on different catalysts. b) The catalytic mechanism on diatomic metal-nitrogen site based on the optimized structures of adsorbed intermediates $COOH^*$ and CO^*. c) Difference in limiting potentials for CO_2 reduction and H_2 evolution on different catalysts.

step for Ni-N-C during CO_2RR.[14] With the introduction of Fe into the system, the significantly lowered Tafel slope of Ni/Fe-N-C indicates the kinetics of this step is greatly enhanced.

To bring theoretical mechanism insight, DFT simulations are further performed to reveal the intrinsic catalytic barrier on catalysts. Figure 4a shows the calculated free energy diagram for CO_2RR to CO, and the models are built based on the EXAFS results. Consistent with previous DFT calculations,[7] the rate-limiting steps of CO_2RR on Ni-N-C and Fe-N-C are $CO_2(g)\rightarrow COOH^*$ and $CO^*\rightarrow CO(g)$, respectively, because of the weak binding of $COOH^*$ on Ni-N-C and the strong binding of CO^* on Fe-N-C. By comparison, the free energy diagram on bare Ni/Fe-N-C is quite similar to that on Fe-N-C with a very negative free energy of -0.65 eV for CO^*, and thus the Fe-Ni dual sites tend to be passivated by strongly bounded CO^* during the CO_2RR process. Considering the geometry structure of the CO-adsorbed Ni-Fe dual center (Figure 4b, ii), it can provide an additional active site either on Fe or Ni for the second CO_2 activation. Therefore, the CO-adsorbed configurations are then taken into account. As seen from Figure 4a, the binding strengths of $COOH^*$ and CO^* on CO-adsorbed Ni/Fe-N-C are weaker compared with bare Ni/Fe-N-C, which increases the free energy barrier of $CO_2(g)\rightarrow COOH^*$ to 0.47 eV, whereas decreases the barrier of $CO^*\rightarrow CO(g)$ to 0.27 eV. As a result, the theoretical overpotential on Ni/Fe-N-C reduces from 0.76 to 0.47 V after CO-adsorption, considerably lowering the catalysis barrier for the CO production. On this basis, the CO_2RR mechanism on bimetal-nitrogen site is established (Figure 4b), where the Fe-Ni dual site is first passivated by strongly bounded

CO^* (i-ii) and then the reduction of CO_2 occurs on the Fe site (ii-iV). Similar post-adsorption phenomenon that facilitate the catalytic process have been observed on HO-Co-N_2[15] and Ir-CO[16].

Given that HER is a dominant competitive reaction upon CO_2RR, the difference between thermodynamic limiting potentials for CO_2RR and HER (donated as $U_L(CO_2)-U_L(H_2)$, U_L is defined as the lowest potential that all reaction steps are downhill in free energy) is significant in understanding the selectivity of catalysts.[17] The calculated free energy diagram for HER is shown in Figure S15. Accordingly, the $U_L(CO_2)-U_L(H_2)$ on CO-adsorbed Ni/Fe-N-C, Ni-N-C and Fe-N-C is compared in Figure 4c. For Ni/Fe-N-C with CO^*, it shows a more positive $U_L(CO_2)-U_L(H_2)$ value (-0.19 V) than that of Fe-N-C (-0.4 V), corresponding to the higher selectivity for CO_2RR. Note that although the $U_L(CO_2)-U_L(H_2)$ value for Ni-N-C is also very positive, the catalytic reaction is blocked by the first proton-coupled electron transfer step, leading to the relatively poor CO_2RR performance. These results are in good agreement with the experimental observations that Ni/Fe-N-C exhibits enhanced activity and selectivity for CO_2RR over Ni-N-C and Fe-N-C.

In summary, we have demonstrated a concept of diatomic catalyst, referred to isolated Ni-Fe sites anchored on nitrogenated carbon, for electrochemical CO_2RR. The catalytically active center is established by combining the structure-sensitive XAS and DFT analyses. Mechanism study reveals that the bimetal nitrogen sites undergo a structural change into a CO-adsorbed moiety upon CO_2 uptake, which substantially reduces the energy barrier for both the formation of intermediate COOH* and the desorption of CO, leading to the outstanding CO_2RR activity. This work opens up enormous possibilities for the rational design of polynary, synergetic SACs, which is readily adaptable for a range of complex catalytic reactions such as CO_2RR, nitrogen reduction reactions and oxygen reduction reactios.

Acknowledgements

W.R. and X.T. contributed equally to this work. The authors are thankful to UNSW Mark Wainwright Analytical Center for providing access to their XRD, SEM, XPS, Raman, NMR and facilities. This research was undertaken with the assistance of resources provided by the National Computing Infrastructure (NCI) facility at the Australian National University; allocated through both the National Computational Merit Allocation Scheme supported by the Australian Government and the Australian Research Council grant LE160100051(Maintaining and enhancing merit-based access to the NCI National Facility, 2016-2018). This work was supported by the Australian Research Council (DP160103107, FT170100224).

Keywords: Single-atom catalyst • diatomic site • metal-nitrogen • electrocatalyst • CO_2 reduction

[1] a) T. T. Zhuang, Z. Q. Liang, A. Seifitokaldani, Y. Li, P. De Luna, T. Burdyny, F. Che, F. Meng, Y. Min, R. Quintero-Bermudez, *Nat. Catal.* **2018**, *1*, 421; b) S. Lin, C. S. Diercks, Y. B. Zhang, N. Kornienko, E. M. Nichols, Y. Zhao, A. R. Paris, D. Kim, P. Yang, O. M. Yaghi, *Science* **2015**, *349*, 1208-1213; c) C. Costentin, M. Robert, J. M. Savéant, *Chem. Soc. Rev.* **2013**, *42*, 2423-2436.

[2] a) C. S. Diercks, Y. Liu, K. E. Cordova, O. M. Yaghi, *Nat. Mater.* **2018**, *17*, 301; b) S. Gao, Y. Lin, X. Jiao, Y. Sun, Q. Luo, W. Zhang, D. Li, J. Yang, Y. Xie, *Nature* **2016**, *529*, 68; c) Y. J. Zhang, V. Sethuraman, R. Michalsky, A. A. Peterson, *ACS Catal.* **2014**, *4*, 3742-3748.

[3] a) Y. Chen, S. Ji, C. Chen, Q. Peng, D. Wang, Y. Li, *Joule* **2018**, *2*, 1242-1264; b) H. Li, L. Wang, Y. Dai, Z. Pu, Z. Lao, Y. Chen, M. Wang, X. Zheng, J. Zhu, W. Zhang, R. Si, C. Ma, J. Zeng, *Nat. Nanotechnol.* **2018**, *13*, 411-417; c) Z. Liang, C. Qu, D. Xia, R. Zou, Q. Xu, *Angew. Chem. Int. Ed.* **2018**, *57*, 9604-9633; d) D. D. Zhu, J. L. Liu, S. Z. Qiao, *Adv. Mater.* **2016**, *28*, 3423-3452; e) T. Zheng, K. Jiang, H. Wang, *Adv. Mater.* **2018**, 1802066.

[4] a) Y. Cheng, S. Zhao, B. Johannessen, J. P. Veder, M. Saunders, M. R. Rowles, M. Cheng, C. Liu, M. F. Chisholm, R. De Marco, H. M. Cheng, S. Z. Yang, S. P. Jiang, *Adv. Mater.* **2018**, *30*, e1706287; b) Y. Pan, R. Lin, Y. Chen, S. Liu, W. Zhu, X. Cao, W. Chen, K. Wu, W. C. Cheong, Y. Wang, L. Zheng, J. Luo, Y. Lin, Y. Liu, C. Liu, J. Li, Q. Lu, X. Chen, D. Wang, Q. Peng, C. Chen, Y. Li, *J. Am. Chem. Soc.* **2018**, *140*, 4218-4221; c) X. Li, W. Bi, M. Chen, Y. Sun, H. Ju, W. Yan, J. Zhu, X. Wu, W. Chu, C. Wu, Y. Xie, *J. Am. Chem. Soc.* **2017**, *139*, 14889-14892; d) C. Zhang, S. Yang, J. Wu, M. Liu, S. Yazdi, M. Ren, J. Sha, J. Zhong, K. Nie, A. S. Jalilov, *Adv. Energy Mater.* **2018**, 1703487; e) K. Jiang, S. Siahrostami, T. Zheng, Y. Hu, S. Hwang, E. Stavitski, Y. Peng, J. Dynes, M. Gangisetty, D. Su, *Energy Environ. Sci.* **2018**, *11*, 893-903.

[5] X. Wang, Z. Chen, X. Zhao, T. Yao, W. Chen, R. You, C. Zhao, G. Wu, J. Wang, W. Huang, J. Yang, X. Hong, S. Wei, Y. Wu, Y. Li, *Angew. Chem.* **2018**, *57*, 1944-1948.

[6] H. B. Yang, S. F. Hung, S. Liu, K. Yuan, S. Miao, L. Zhang, X. Huang, H.-Y. Wang, W. Cai, R. Chen, *Nat. Energy* **2018**, *3*, 140.

[7] W. Ju, A. Bagger, G. P. Hao, A. S. Varela, I. Sinev, V. Bon, B. Roldan Cuenya, S. Kaskel, J. Rossmeisl, P. Strasser, *Nat. Commun.* **2017**, *8*, 944.

[8] J. Jiao, R. Lin, S. Liu, W.-C. Cheong, C. Zhang, Z. Chen, Y. Pan, J. Tang, K. Wu, S.-F. Hung, H. M. Chen, L. Zheng, Q. Lu, X. Yang, B. Xu, H. Xiao, J. Li, D. Wang, Q. Peng, C. Chen, Y. Li, *Nat. Chem.* **2019**. doi.org/10.1038/s41557-018-0201-x.

[9] F. Pan, H. Zhang, K. Liu, D. Cullen, K. More, M. Wang, Z. Feng, G. Wang, G. Wu, Y. Li, *ACS Catal.* **2018**, *8*, 3116-3122.

[10] a) C. Zhao, X. Dai, T. Yao, W. Chen, X. Wang, J. Wang, J. Yang, S. Wei, Y. Wu, Y. Li, *J. Am. Chem. Soc.* **2017**, *139*, 8078-8081; b) X. C. Huang, Y. Y. Lin, J. P. Zhang, X. M. Chen, *Angew. Chem. Int. Ed.* **2006**, *45*, 1557-1559.

[11] a) S. Kabir, K. Artyushkova, B. Kiefer, P. Atanassov, *Phys. Chem. Chem. Phys.* **2015**, *17*, 17785-17789; b) K. Artyushkova, B. Kiefer, B. Halevi, A. Knop-Gericke, R. Schlogl, P. Atanassov, *Chem. Commun.* **2013**, *49*, 2539-2541.

[12] T. Yamamoto, *X-Ray Spectrom.* **2008**, *37*, 572-584.

[13] a) C. Yan, H. Li, Y. Ye, H. Wu, F. Cai, R. Si, J. Xiao, S. Miao, S. Xie, F. Yang, *Energy Environ. Sci.* **2018**, *11*, 1204-1210; b) J. Wang, Z. Huang, W. Liu, C. Chang, H. Tang, Z. Li, W. Chen, C. Jia, T. Yao, S. Wei, Y. Wu, Y. Li, *J. Am. Chem. Soc.* **2017**, *139*, 17281-17284.

[14] M. Gattrell, N. Gupta, A. Co, *J. Electroanal. Chem.* **2006**, *594*, 1-19.

[15] L. Cao, Q. Luo, W. Liu, Y. Lin, X. Liu, Y. Cao, W. Zhang, Y. Wu, J. Yang, T. Yao, S. Wei, *Nat. Catal.* **2018**. doi.org/10.1038/s41929-018-0203-5.

[16] Y. Lu, J. Wang, L. Yu, L. Kovarik, X. Zhang, A. S. Hoffman, A. Gallo, S. R. Bare, D. Sokaras, T. Kroll, *Nat. Catal.* **2018**, 1.

[17] a) D. Kim, C. Xie, N. Becknell, Y. Yu, M. Karamad, K. Chan, E. J. Crumlin, J. K. Nørskov, P. Yang, *J. Am. Chem. Soc.* **2017**, *139*, 8329-8336; b) C. Shi, H. A. Hansen, A. C. Lausche, J. K. Nørskov, *Phys. Chem. Chem. Phys.* **2014**, *16*, 4720-4727.

Isolated diatomic Ni-Fe sites anchored on nitrogenated carbon is developed. On the strength of this collaborative coordination, the catalysts achieve an ultrahigh Faradaic efficiency of 98% at -0.7 V, outstanding turnover frequency, as well as robust electrode durability for electrochemical CO_2 reduction.

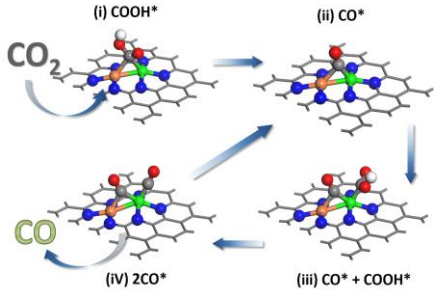

*Wenhao Ren,[†] Xin Tan,[†] Wanfeng Yang, Chen Jia, Sean C. Smith and Chuan Zhao**

Page No. – Page No.

Isolated Diatomic Ni-Fe Metal-Nitrogen Sites for Synergistic Electroreduction of CO_2